

Ultrafast nonlinear phonon response of few-layer hexagonal boron nitrideTaehee Kang , Jia Zhang , Achintya Kundu , Klaus Reimann , Michael Woerner, and Thomas Elsaesser **Max-Born-Institut für Nichtlineare Optik und Kurzzeitspektroskopie, 12489 Berlin, Germany*Bernard Gil and Guillaume Cassabois *Laboratoire Charles Coulomb (L2C), UMR 5221 CNRS-Université de Montpellier, F-34095 Montpellier, France*

Christos Flytzanis

*Laboratoire de Physique, École Normale Supérieure, Université PSL, F-75231 Paris, France*Giorgia Fugallo *CNRS, UMR 6607, Laboratoire de Thermique et Energie de Nantes (LTen) Polytech'Nantes, Université de Nantes, F-44306 Nantes, France*Michele Lazzeri *Sorbonne Université, CNRS UMR 7590, MNHN, IMPMC, F-75005 Paris, France*

Ryan Page and Debdeep Jena

Cornell University, Department of Materials Science and Engineering, Ithaca, New York 14853, USA

(Received 22 February 2021; revised 2 June 2021; accepted 20 September 2021; published 11 October 2021)

Nonequilibrium dynamics of transverse-optical (TO) phonons and low-frequency interlayer shear and breathing modes are mapped in femtosecond midinfrared pump-probe experiments. Time-resolved changes of TO phonon absorption reveal a TO phonon lifetime of 1.2 ps, while low-frequency excitations decay with a time constant of 22 ps. The coupling of intralayer TO and interlayer motions manifests in a quasi-instantaneous redshift of the TO phonon resonance by some 10 cm^{-1} . Theoretical calculations account for the coupling scenario and underline the relevance of interphonon interactions for the nonlinear phonon response.

DOI: [10.1103/PhysRevB.104.L140302](https://doi.org/10.1103/PhysRevB.104.L140302)

The crystal structure of hexagonal boron nitride (hBN) consists of covalently bound six-rings of boron and nitrogen atoms arranged in two-dimensional layers [1]. Adjacent layers are coupled via much weaker van der Waals interactions, making the material highly anisotropic. Mono- and few-layer hBN have received strong interest as a prototypical quasi-two-dimensional quantum material [2], holding strong potential for synthesizing van der Waals heterostructures [3] and applications in optoelectronics [4], nanophotonics, and phonon polaritonics [5]. The electronic structure [6,7] and the linear and nonlinear optical properties [8,9] of few-layer hBN have been studied in some detail, whereas insight into carrier and phonon dynamics has remained very limited [10].

The anisotropic structure of hBN results in distinctly different frequencies of phonons connected with intraplane and interplane atomic motions. Phonon modes of bulk hBN have been studied by infrared and Raman spectroscopy [11–15], inelastic x-ray scattering [13], and theoretical calculations [16,17]. At the Γ point ($q = 0$), the infrared-active transverse-optical (TO) phonon of E_{1u} symmetry displays a frequency of 1367 cm^{-1} ($E_{\text{TO}} = 169.5 \text{ meV}$), nearly identical to a Raman-active phonon of E_{2g} symmetry. Both modes are connected

with different in-plane atomic motions, as shown for the TO phonon in Fig. 1(a) (inset). Second-order Raman spectra suggest a TO phonon anharmonicity on the order of 5 cm^{-1} [13].

Lifetimes of the TO phonon of bulk hBN have been estimated from the damping term in numerical line shape fits of the reststrahlen band, giving values from 0.8 to 1.3 ps for samples with the natural isotope variation of boron [5,15,18]. An analysis of the Raman line shapes of the E_{2g} mode at 1367 cm^{-1} suggests a similar lifetime of 0.7 to 1 ps. For both modes, similar decay channels mediated via three- and four-phonon anharmonic couplings have been proposed [18].

Motions of the stacked BN planes relative to each other give rise to rigid-plane shear and breathing/compression modes at low energy. In bulk hBN, the Raman-active horizontally polarized rigid-plane shear mode arises at 54 cm^{-1} ($E_{\text{SH}} = 6.74 \text{ meV}$). In hBN with a finite number N of BN layers, the discretization of the k -vector perpendicular to the layers results in an increasing number of optical phonon branches. Theory [16,17] predicts a splitting of the bulk rigid-plane modes in $N - 1$ breathing modes and $N - 1$ doubly degenerate shear modes, the latter at energies below E_{SH} . So far, experimental results on such modes are very limited [19] and couplings of intralayer and interlayer modes unknown.

*elsasser@mbi-berlin.de

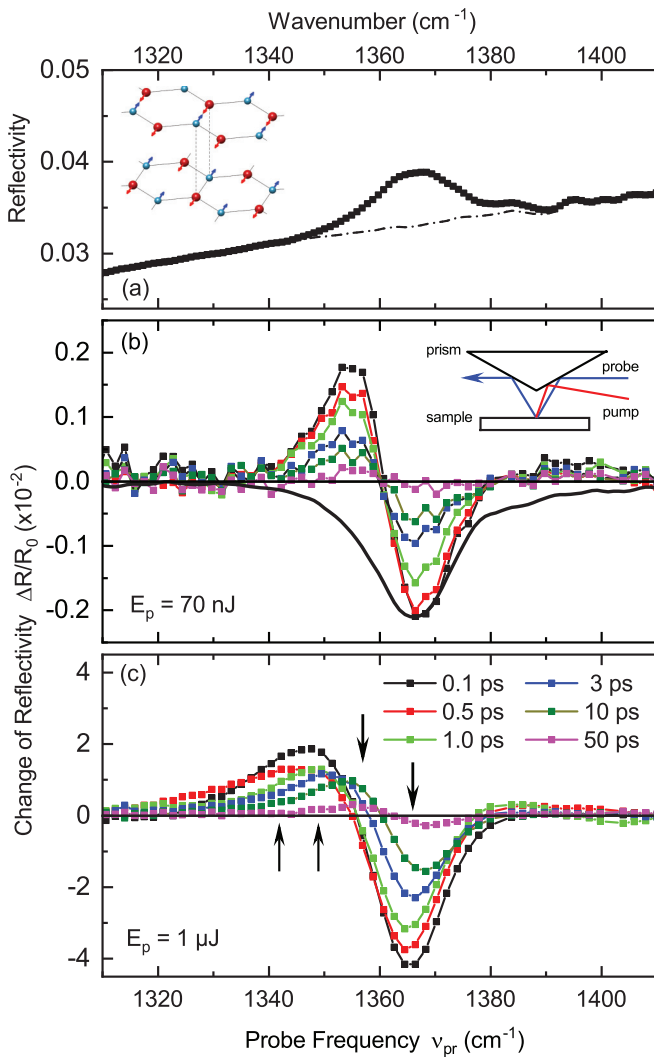


FIG. 1. (a) Reflectivity spectrum of the few-layer hexagonal boron nitride (hBN) sample in the range of the transverse-optical (TO) phonon resonance at 1366 cm^{-1} (symbols). Dash-dotted line: Experimental reflectivity spectrum of the sapphire substrate. Inset: Atomic elongations connected with the TO phonon of hBN. (b) Transient reflectivity spectra (symbols) measured with a pump energy $E_p = 70$ nJ. The change of reflectivity $\Delta R/R_0 = (R - R_0)/R_0$ is plotted as a function of probe frequency for different delay times (R, R_0 : reflectivity of the sample with and without excitation). Solid lines are to guide the eye. The thick solid line gives the inverted and scaled reflectivity spectrum from panel (a) after subtraction of the substrate reflectivity. Inset: Pump-probe geometry applied in the experiments. (c) Same as (b) for a pump energy $E_p = 1.0$ μ J. The arrows mark the probe frequencies at which the transients in Fig. 2 were recorded.

For a basic physical understanding of the low-frequency dielectric properties of hBN and applications in phonon polaritonics, insight into phonon-phonon interactions and the resulting nonequilibrium dynamics is mandatory. Moreover, coupled phonon excitations are relevant for energy relaxation and heat transport, including the interplay of in-plane and interplane motions. In this paper, we study the nonlinear phonon response of few-layer hBN. Upon femtosecond midinfrared excitation via the TO phonon absorption band, the resulting

ultrafast dynamics exhibits both a pronounced coupling of interlayer and TO phonon modes and population relaxation processes of the coupled modes on different time scales. The anharmonic phonon-phonon coupling is accounted for by in-depth theoretical calculations.

The few-layer hBN sample studied here was grown directly on a sapphire substrate and has an average thickness of 2.5 nm, corresponding to $N = 8$ -9 hBN layers [20]. For such N , both the rigid-plane shear and some breathing phonons are expected at frequencies below the bulk shear mode at 54 cm^{-1} [17,19]. A temporally and spectrally resolved pump-probe approach with femtosecond midinfrared pulses is employed to map nonequilibrium phonon dynamics. As depicted schematically in Fig. 1(b) (inset), the s -polarized (TE) pump and probe pulses were reflected from a gold-coated prism and hit the sample under slightly different angles of incidence. The probe beam reflected from the sample passed the second facet of the prism, was spectrally dispersed in a monochromator, and detected with a 64-element HgCdTe detector array (spectral resolution 2 cm^{-1}). A reference pulse reflected from an unexcited part of the sample was detected by a second array. Details of sample preparation, interaction geometry, and mid-infrared pulse generation are presented in the Supplemental Material [21] (see also Refs. [22–26] therein).

The linear reflectivity spectrum [Fig. 1(a)] of the hBN sample exhibits the TO phonon resonance at 1366 cm^{-1} , in agreement with an attenuated total reflection spectrum of the sample (Fig. S2 in the Supplemental Material [21]). The width of the resonance has a value $\Delta\nu_{\text{TO}} \approx 15\text{ cm}^{-1}$, which is about twice as large as values derived from the reststrahlen band of high-quality bulk hBN. We assign this discrepancy to structural imperfections of the few-layer sample. A more detailed analysis of the reflectivity spectrum is presented in Ref. [21].

In Figs. 1(b) and 1(c), pump-probe spectra measured with pump energies $E_p = 70$ nJ and $1.0\text{ }\mu\text{J}$ are summarized (symbols). The change of reflectivity $\Delta R/R_0$ is plotted as a function of probe frequency ν_{pr} for the delay times given in panel (c). From the pump fluence and the TO phonon absorption of the sample, one estimates an excitation density of $6.5 \times 10^{19}\text{ cm}^{-3}$ for $E_p = 70$ nJ and $9.5 \times 10^{20}\text{ cm}^{-3}$ for $E_p = 1.0\text{ }\mu\text{J}$. Both numbers are much smaller than the TO phonon density of states of $\sim 5 \times 10^{22}\text{ cm}^{-3}$, as estimated from an Einstein model. Thus, multiple excitations to higher TO phonon states are negligible.

All transient spectra display a decrease of reflectivity at high probe frequencies, corresponding to an absorption decrease, and an increase of reflectivity/absorption at low probe frequencies. The spectra for $E_p = 70$ nJ [Fig. 1(b)] are of a dispersive shape, which is similar for all time delays and within the TO phonon line observed in linear reflectivity [thick solid line in panel (b)]. In contrast, the spectral envelope of the positive and negative ΔR and the position of the zero crossing change with delay time for the higher $E_p = 1\text{ }\mu\text{J}$ [Fig. 1(c)].

The time-resolved pump-probe traces shown in Fig. 2 were recorded at the probe frequencies marked by arrows in Fig. 1(c). Around delay zero, the transients show a fast modulation originating from nonlinear cross-phase modulation of pump and probe pulses. All transients measured with $E_p = 70$ nJ [Fig. 2(a)] exhibit a biphasic decay with relative

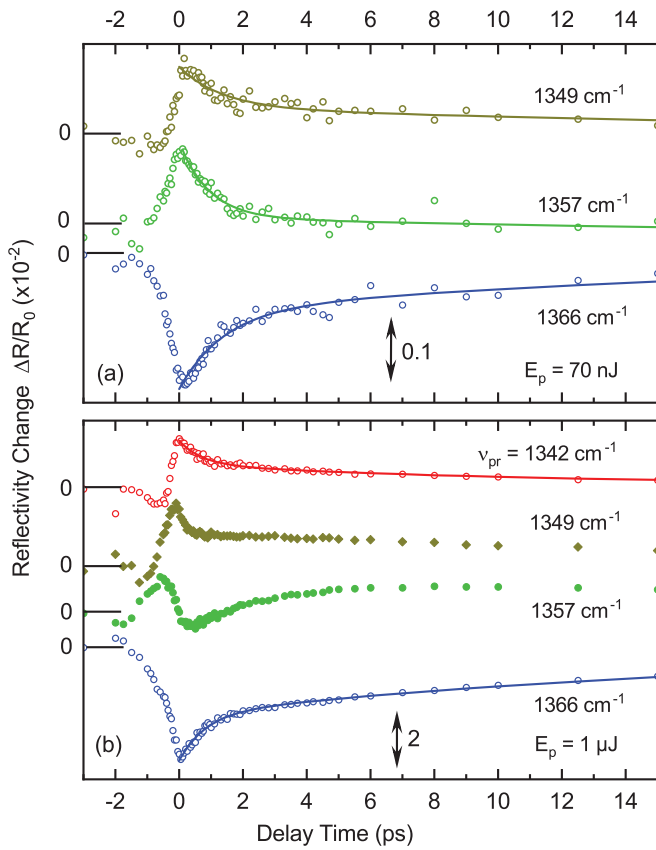


FIG. 2. (a) Time-resolved pump-probe traces recorded at fixed probe frequencies ν_{pr} [cf. arrows in Fig. 1(c)] with a pump energy $E_p = 70$ nJ (symbols). The change of reflectivity $\Delta R/R_0$ is plotted as a function of pump-probe delay. The solid lines are numerical fits to the data and represent biexponential decays with time constants of 1.2 and 22 ps. (b) Same for $E_p = 1.0$ μ J.

amplitudes depending on probe frequency. Such kinetics are reproduced by fitting two instantly rising contributions with decay times of 1.2 ± 0.3 and 22 ± 5 ps to the data points [solid lines in Figs. 2(a) and 2(b)]. The long decay time was validated by data extending to delay times of 60 ps (see Fig. S3 in the Supplemental Material [21]). The transients recorded with $E_p = 1$ μ J reveal a more complex kinetic behavior. The decays observed at $\nu_{pr} = 1342$ and 1366 cm^{-1} follow biexponential decays with time constants close to the data for $E_p = 70$ nJ. In contrast, the reflectivity changes at $\nu_{pr} = 1349$ and 1357 cm^{-1} are not accounted for by ratelike kinetics. This fact reflects the reshaping of the pump-probe spectra [cf. Fig. 1(c)] and the frequency shift of the zero crossing with delay time.

Experiments with pump pulses of a reduced bandwidth $\Delta\nu_p$ give additional insight in the nonlinear phonon response. The pump energy E_p was adjusted to implement a similar excitation level for $\Delta\nu_p = 20, 32, 54,$ and 200 cm^{-1} [full width at half maximum (FWHM)]. Pump-probe spectra for a delay time $t_D = 3$ ps after the fast signal decay [Fig. 3(a)] display identical envelopes for the different $\Delta\nu_p$. The time evolution of reflectivity changes at a fixed probe frequency (not shown) is independent from $\Delta\nu_p$ as well. In Fig. 3(b), the frequency positions of the positive and negative peaks in the

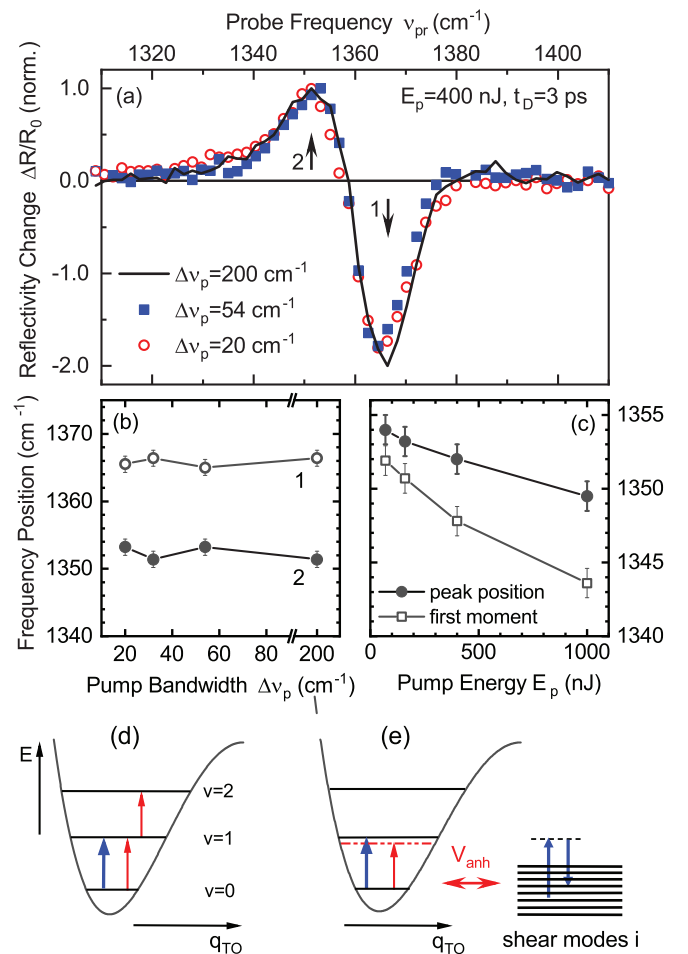


FIG. 3. Pump-probe spectra at a delay $t_D = 3$ ps recorded with pump bandwidths $\Delta\nu_p$. The spectra are normalized to the maximum positive $\Delta R/R_0$. The pump energy was $E_p = 400$ nJ for $\Delta\nu_p = 200$ cm^{-1} . For a reduced $\Delta\nu_p$, E_p was adjusted to make the amount of absorbed pump energy identical to the data for $E_p = 400$ nJ. (b) Frequency positions of the maximum (1) negative and (2) positive reflectivity changes as a function of $\Delta\nu_p$. (c) Peak position and first moment of the positive reflectivity change as a function of E_p for excitation with $\Delta\nu_p = 200$ cm^{-1} . (d) Schematic of the anharmonic transverse-optical (TO) phonon potential along the coordinate q_{TO} with optical transitions relevant for excitation (blue arrow) and probing (red arrows). (e) Anharmonic TO phonon potential along q_{TO} and vibrational levels of low-frequency shear (and breathing) modes i with a Raman excitation process (blue arrows). The TO phonon and shear modes are anharmonically coupled via V_{anh} .

spectra for $t_D = 3$ ps are plotted vs $\Delta\nu_p$. Figure 3(c) shows the frequency position of the positive peak (solid symbols) and the first moment $M = [\int \nu g(\nu) d\nu] / \int g(\nu) d\nu$ of the redshifted positive component $g(\nu)$ of the pump-probe spectra as a function of E_p (open symbols). Both quantities exhibit a redshift increasing roughly linearly with E_p .

We now discuss the mechanisms behind the ultrafast nonlinear phonon response with the support of first-principles evaluations [27–29] of phonon lifetimes, anharmonic frequency shifts, and interphonon anharmonic couplings [30,36,37]. The theoretical methods are described in Ref. [21]. We recall that the TO phonon potential energy

surface shows a small anharmonicity along the q_{TO} coordinate of 5 cm^{-1} [13]. As schematically shown in Fig. 3(d), this anharmonicity leads to a redshift of the $v = 1$ to 2 compared with the fundamental $v = 0$ -to-1 transition. Resonant excitation by the pump pulses [blue arrow in Fig. 3(d)] results in a population decrease in the $v = 0$ and an increase in the $v = 1$ TO phonon state. Concomitantly, the absorption/reflectivity on the $v = 0$ -to-1 transition decreases due to depopulation of the $v = 0$ state and stimulated emission from the $v = 1$ state. In parallel, a redshifted absorption/reflectivity increase arises on the $v = 1$ -to-2 transition. The probe pulse [red arrows in Fig. 3(d)] maps such changes.

The dispersive shape of the transient spectra in Figs. 1(b) and 1(c) is in line with this picture. For a pump energy $E_p = 70 \text{ nJ}$, all reflectivity changes occur within the steady-state TO phonon peak [thick solid line in Fig. 1(b)], reflecting the small diagonal anharmonicity. The time-resolved transients in Fig. 2(a) display a first decay time of 1.2 ps, which we assign to the population decay of the $v = 1$ state of the TO phonon. The 1.2-ps decay measured here directly supports indirect lifetime estimates from vibrational linewidths [5, 18]. For $E_p = 1 \text{ }\mu\text{J}$, one observes a similar 1.2-ps decay at $\nu_{pr} = 1342$ and 1366 cm^{-1} .

Relaxation of the $v = 1$ TO phonon population is connected with a population transfer to anharmonically coupled phonons at lower frequency [14, 15, 18]. The theoretical calculations of Ref. [18] suggest a predominant 4-phonon decay channel, invoking the zone-center A_{2u} phonon at 820 cm^{-1} and out-of-plane optical/acoustic phonons at the M and K points of the Brillouin zone (BZ) with frequencies $\sim 300 \text{ cm}^{-1}$. A relaxation scheme and more detailed discussion based on our calculations is presented in Ref. [21]. The calculated TO phonon lifetimes of 1 ps [18] and 1.78 ps [21] are close to the experimental value of 1.2 ps.

The pump-probe spectra (Fig. 1) display a redshift of the fundamental ($v = 0$ to 1) TO phonon absorption even after the decay of the TO $v = 1$ population, i.e., with the TO phonons in their $v = 0$ state. The nonexponential time-resolved transients measured with $E_p = 1 \text{ }\mu\text{J}$ at $\nu_{pr} = 1349$ and 1357 cm^{-1} [Fig. 2(b)] demonstrate the onset of this redshift at early delays during the decay of the $v = 1$ state and, together with all other transients in Fig. 2, their decay with a time constant of 22 ps. The redshift of the TO phonon transition is due to the intermode anharmonic coupling to a subset of low-frequency phonons excited by the pump pulse. As sketched in Fig. 3(e), a Raman process, which is resonantly enhanced by the TO transition dipole, excites low-frequency Raman-active phonons i . This excitation mechanism is nonselective and generates excess populations of all Raman-active modes within the pump bandwidth. The nonequilibrium populations of low-frequency modes redshift the TO phonon transition via the anharmonic coupling V_{anh} . The redshift at a delay $t_D = 3$ ps after the TO phonon decay scales with the pump energy E_p [Fig. 3(c)], i.e., the generated excess population, and decays with a time constant of 22 ps by population relaxation of the low-frequency phonon states.

The experiments with reduced pump bandwidth $\Delta\nu_p$ (Fig. 3) show that the redshift at $t_D = 3$ ps scales with E_p but not with $\Delta\nu_p$. The data for $\Delta\nu_p = 20 \text{ cm}^{-1}$ (FWHM),

however, set an upper limit of $30\text{--}40 \text{ cm}^{-1}$ for the frequency of the phonons inducing the redshift. While optically accessible phonons $< 50 \text{ cm}^{-1}$ are absent in bulk hBN, a subset of Raman active interlayer shear modes i and one or two breathing modes of few-layer hBN shows $< 40 \text{ cm}^{-1}$ frequencies [17, 21]. The observed TO redshift is assigned to a coupling with such low-frequency phonons in which nonequilibrium populations are generated by the Raman pump mechanism. Independent evidence for the existence of low-frequency shear and breathing modes comes from the Raman spectra of Ref. [19], displaying a broad low-frequency phonon signal superimposed by the strongest sharp Raman line at the highest shear-mode frequency [38].

This picture relies on the concept that, due to optical selection rules, the pump pulse excites only phonons with zero wave vector, i.e., in an infinitesimally small volume in the BZ. If we indicate the phonon population as $n(\mathbf{q})$, where \mathbf{q} is the wave vector, immediately after the pump excitation, we have $n(\mathbf{q}) = n_0(\mathbf{q}) + A\delta(\mathbf{q})$, where $n_0(\mathbf{q})$ is the thermal ($T = 300 \text{ K}$) population, and δ is the Dirac distribution [39]. Such a distribution does not alter the phonon lifetimes, which are determined by the population distribution over all the BZ (and not by what happens only at $\mathbf{q} = 0$). However, it can induce a frequency shift of the TO mode through anharmonic coupling with the low-energy shear and breathing modes at the BZ center. Interestingly, in bulk hBN, the TO and the low-energy shear modes are weakly coupled, with a predominant contribution of 4-phonon processes and a coupling term of the order of -0.02 cm^{-1} . With this weak coupling, to experimentally observe a TO shift $\Delta\nu_{\text{TO}} = 10 \text{ cm}^{-1}$, we must assume $A \approx \Delta\nu_{\text{TO}}/(0.02 \text{ cm}^{-1}) \sim 500$. For the bulk $E_{\text{SH}} = 6.7 \text{ meV}$, this value of A corresponds to an effective energy per unit cell of $\sim 1 \text{ eV}$ to be provided by the pump pulse, a value prohibitively high under the present experimental conditions.

On the contrary, the generation of a TO shift $\Delta\nu_{\text{TO}} = 10 \text{ cm}^{-1}$ becomes possible when passing from bulk to few-layer hBN. Our calculations show that the coupling term displays a strong dispersion along the c axis and increases up to two orders of magnitude. For a maximum phonon frequency of $30\text{--}40 \text{ cm}^{-1}$ (cf. Fig. 3), such strong coupling to shear and breathing modes shrinks the excitation energy required per unit cell to $\sim 20 \text{ meV}$, well in the range of the experiment. Our picture is further supported by the calculated lifetime of the low-energy shear modes of $\tau_{\text{SH}} = 25 \text{ ps}$, close to the experimental decay time of 22 ps. The large difference between τ_{SH} and the 1.2-ps TO phonon lifetime assures, as experimentally observed, that the TO nonlinear signal decreases while the redshift remains the same during the TO decay time.

In conclusion, the ultrafast nonlinear phonon response of few-layer hBN reveals a TO phonon lifetime of 1.2 ps and a 22-ps decay time of low-frequency phonons. Nonequilibrium populations of rigid-plane shear and breathing modes induce a transient redshift of the TO phonon resonance, a direct manifestation of the anharmonic coupling between the TO intralayer and interlayer degrees of freedom. This coupling is highly relevant for future extensions of phonon polaritonics into the nonlinear regime.

- [1] R. S. Pease, Crystal structure of boron nitride, *Nature (London)* **165**, 722 (1950).
- [2] Y. Shi, C. Hamsen, X. Jia, K. Kang Kim, A. Reina, M. Hofmann, A. Long Hsu, K. Zhang, H. Li, Z.-Y. Juang, M. S. Dresselhaus, L.-J. Li, and J. Kong, Synthesis of few-layer hexagonal boron nitride thin film by chemical vapor deposition, *Nano Lett.* **10**, 4134 (2010).
- [3] A. K. Geim and I. V. Grigorieva, Van der Waals heterostructures, *Nature (London)* **499**, 419 (2013).
- [4] J. D. Caldwell, I. Aharonovich, G. Cassaboïs, J. H. Edgar, B. Gil, and D. N. Basov, Photonics with hexagonal boron nitride, *Nat. Rev. Mater.* **4**, 552 (2019).
- [5] A. J. Giles, S. Dai, I. Vurgaftman, T. Hoffman, S. Liu, L. Lindsay, C. T. Ellis, N. Assefa, I. Chatzakis, T. L. Reinicke, J. G. Tischler, M. M. Fogler, J. H. Edgar, D. N. Basov, and J. D. Caldwell, Ultralow-loss polaritons in isotopically pure boron nitride, *Nat. Mater.* **17**, 134 (2018).
- [6] G. Cassaboïs, P. Valvin, and B. Gil, Hexagonal boron nitride is an indirect bandgap semiconductor, *Nat. Photonics* **10**, 262 (2016).
- [7] L. Schué, L. Sponza, A. Plaud, H. Bensalah, K. Watanabe, T. Taniguchi, F. Ducastelle, A. Loiseau, and J. Barjon, Bright Luminescence from Indirect and Strongly Bound Excitons in h-BN, *Phys. Rev. Lett.* **122**, 067401 (2019).
- [8] Y. Li, Y. Rao, K. F. Mak, Y. You, S. Wang, C. R. Dean, and T. F. Heinz, Probing symmetry properties of few-layer MoS₂ and h-BN by optical second-harmonic generation, *Nano Lett.* **13**, 3329 (2013).
- [9] C.-J. Kim, L. Brown, M. W. Graham, R. Hovden, R. W. Havener, P. L. McEuen, D. A. Muller, and J. Park, Stacking order dependent second harmonic generation and topological defects in h-BN bilayers, *Nano Lett.* **13**, 5660 (2013).
- [10] D. Golla, A. Brasington, B. J. LeRoy, and A. Sandhu, Ultrafast relaxation of hot phonons in graphene-hBN heterostructures, *APL Mater.* **5**, 056101 (2017).
- [11] R. Geick, C. H. Perry, and G. Rupprecht, Normal modes in hexagonal boron nitride, *Phys. Rev.* **146**, 543 (1966).
- [12] S. Reich, A. C. Ferrari, R. Arenal, A. Loiseau, I. Bello, and J. Robertson, Resonant Raman scattering in cubic and hexagonal boron nitride, *Phys. Rev. B* **71**, 205201 (2005).
- [13] J. Serrano, A. Bosak, R. Arenal, M. Krisch, K. Watanabe, T. Taniguchi, H. Kanda, A. Rubio, and L. Wirtz, Vibrational Properties of Hexagonal Boron Nitride: Inelastic X-Ray Scattering and *Ab-initio* Calculations, *Phys. Rev. Lett.* **98**, 095503 (2007).
- [14] R. Cuscó, B. Gil, G. Cassaboïs, and L. Artús, Temperature dependence of Raman-active phonons and anharmonic interactions in layered hexagonal BN, *Phys. Rev. B* **94**, 155435 (2016).
- [15] R. Cuscó, L. Artús, J. H. Edgar, S. Liu, G. Cassaboïs, and B. Gil, Isotope effects on phonon anharmonicity in layered van der Waals crystals: isotopically pure hexagonal boron nitride, *Phys. Rev. B* **97**, 155435 (2018).
- [16] K. H. Michel and B. Verberck, Phonon dispersions and piezoelectricity in bulk and multilayers of hexagonal boron nitride, *Phys. Rev. B* **83**, 115328 (2011).
- [17] K. H. Michel and B. Verberck, Theory of rigid-plane phonon modes in layered crystals, *Phys. Rev. B* **85**, 094303 (2012).
- [18] A. Segura, R. Cuscó, T. Taniguchi, K. Watanabe, and L. Artús, Long lifetime of the E_{1u} in-plane infrared-active modes of h-BN, *Phys. Rev. B* **101**, 235203 (2020).
- [19] I. Stenger, L. Schué, M. Boukhicha, B. Berini, B. Plaçais, L. Loiseau, and J. Barjon, Low frequency Raman spectroscopy of few-atomic-layer thick hBN crystals, *2D Mater.* **4**, 031003 (2017).
- [20] R. Page, J. Casamento, Y. Cho, S. Rouvimov, H. G. Xing, and D. Jena, Rotationally aligned hexagonal boron nitride on sapphire by high-temperature molecular beam epitaxy, *Phys. Rev. Mater.* **3**, 064001 (2019).
- [21] See Supplemental Material at <http://link.aps.org/supplemental/10.1103/PhysRevB.104.L140302> for sample preparation and characterization, experimental methods, additional pump-probe results, and computational approach.
- [22] J. D. Caldwell, A. V. Kretinin, Y. Chen, V. Giannini, M. M. Fogler, Y. Francescato, C. T. Ellis, J. G. Tischler, C. R. Woods, A. J. Giles, M. Hong, K. Watanabe, T. Taniguchi, S. A. Maier, and K. S. Novoselov, Sub-diffractive volume-confined polaritons in the natural hyperbolic material hexagonal boron nitride, *Nat. Commun.* **5**, 5221 (2014).
- [23] N. E. Levinger, R. Costard, E. T. J. Nibbering, and T. Elsaesser, Ultrafast energy migration pathways in self-assembled phospholipids interacting with confined water, *J. Phys. Chem. A* **115**, 11952 (2011).
- [24] B. B. Karki, R. M. Wentzcovitch, S. de Gironcoli, and S. Baroni, High-pressure lattice dynamics and thermoelasticity of MgO, *Phys. Rev. B* **61**, 8793 (2000).
- [25] S. I. Tamura, Isotope scattering of dispersive phonons in Ge, *Phys. Rev. B* **27**, 858 (1983).
- [26] M. Lazzeri and F. Mauri, First-Principles Calculation of Vibrational Raman Spectra in Large Systems—Signature of Small Rings in Crystalline SiO₂, *Phys. Rev. Lett.* **90**, 036401 (2003).
- [27] P. Hohenberg and W. Kohn, Inhomogeneous electron gas, *Phys. Rev.* **136**, B864 (1964).
- [28] W. Kohn and L. J. Sham, Self-consistent equations including exchange and correlation effects, *Phys. Rev.* **140**, A1133 (1965).
- [29] S. Baroni, S. de Gironcoli, A. Dal Corso, and P. Giannozzi, Phonons and related crystal properties from density-functional perturbation theory, *Rev. Mod. Phys.* **73**, 515 (2001).
- [30] DFT calculations were done with the QUANTUMESPRESSO package [31] within pseudopotential [32] and the local density approximation [33] (110 Ry plane-waves cutoff and 12 × 12 × 8 shifted electronic integration grid). Phonon frequencies were obtained on a mesh 8 × 8 × 6 grid of *k* points and interpolated to arbitrary wave vectors for the calculation of phonon dispersion and phonon density of states. All the scatterings were first calculated on a 4 × 4 × 2 phonon wave vectors grid and then Fourier interpolated on a 100 × 100 × 100 grid (the procedure is described in detail in Refs. [34,35]).
- [31] P. Giannozzi, O. Andreussi, T. Brumme, O. Bunau, M. B. Nardelli, M. Calandra, R. Car, C. Cavazzoni, D. Ceresoli, M. Cococcioni, N. Colonna, I. Carnimeo, A. D. Corso, S. de Gironcoli, P. Delugas, R. DiStasio, A. Ferretti, A. Floris, G. Fratesi, G. Fugallo, R. Gebauer, U. Gerstmann *et al.*, Advanced capabilities for materials modelling with QUANTUMESPRESSO, *J. Phys.: Condens. Matter* **29**, 465901 (2017).
- [32] N. Troullier and J. L. Martins, Efficient pseudopotentials for plane-wave calculations, *Phys. Rev. B* **43**, 1993 (1991).
- [33] J. P. Perdew and A. Zunger, Self-interaction correction to density-functional approximations for many-electron systems, *Phys. Rev. B* **23**, 5048 (1981).

- [34] M. Lazzeri and S. de Gironcoli, First-principles study of the thermal expansion of Be(10 $\bar{1}$ 0), *Phys. Rev. B* **65**, 245402 (2002).
- [35] L. Paulatto, F. Mauri, and M. Lazzeri, Anharmonic properties from a generalized third-order *ab initio* approach: theory and applications to graphite and graphene, *Phys. Rev. B* **87**, 214303 (2013).
- [36] M. Lazzeri, M. Calandra, and F. Mauri, Anharmonic phonon frequency shift in MgB₂, *Phys. Rev. B* **68**, 220509(R) (2003).
- [37] G. Fugallo, B. Rousseau, and M. Lazzeri, Infrared reflectance, transmittance, and emittance spectra of MgO from first principles, *Phys. Rev. B* **98**, 184307 (2018).
- [38] L. Liang, A. A. Puretzky, B. G. Sumpter, and V. Meunier, Interlayer bond polarizability model for stacking-dependent low-frequency Raman scattering in layered materials, *Nanoscale* **9**, 15340 (2017).
- [39] A is basically a phonon population resulting from Bose-Einstein statistics for a 50 cm⁻¹ phonon.

Supplemental Material: Ultrafast nonlinear phonon response of few-layer hexagonal boron nitride

Taehee Kang, Jia Zhang, Achintya Kundu, Klaus Reimann, Michael Woerner, and Thomas Elsaesser*
Max-Born-Institut für Nichtlineare Optik und Kurzzeitspektroskopie, 12489 Berlin, Germany

Bernard Gil and Guillaume Cassabois
Laboratoire Charles Coulomb (L2C), UMR 5221 CNRS-Université de Montpellier, F-34095 Montpellier, France

Christos Flytzanis
Laboratoire de Physique, École Normale Supérieure, Université PSL, F-75231 Paris, France

Giorgia Fugallo
CNRS, UMR 6607, Laboratoire de Thermique et Energie de Nantes (LTeN) Polytech'Nantes, Université de Nantes, F-44306, Nantes, France

Michele Lazzeri
Sorbonne Université, CNRS UMR 7590, MNHN, IMPMC, F-75005 Paris, France

Ryan Page and Debdeep Jena
Cornell University, Department of Materials Science and Engineering, Ithaca, New York 14853, USA
 (Dated: August 21, 2021)

SAMPLE PREPARATION AND CHARACTERIZATION

The few-layer hBN sample was grown directly on a sapphire substrate by high temperature molecular beam epitaxy [1] and characterized by atomic force microscopy, Raman, and optical absorption spectroscopy. It has an average thickness of 2.5 nm, corresponding to 8 to 9 hBN layers for which the rigid-plane shear phonons are expected at frequencies below the bulk shear mode at 54 cm^{-1} . The sample homogeneity over an area up to 1 cm^2 was confirmed by spatially resolved second-harmonic generation (Fig. S1). The second harmonic was generated with femtosecond pulses centered at 1060 nm and focused to a spot size of few micrometers. The small spread of second-harmonic intensity points to a high structural homogeneity on the several tens of micrometer length scale of the area excited by femtosecond pulses.

LINEAR REFLECTIVITY SPECTRUM

Infrared reflectivity spectra of the sample and a bare sapphire substrate, both at $T = 300 \text{ K}$, were recorded with an FTIR spectrometer (Bruker Vertex 80, incidence angle 45° , unpolarized). Figure S2(a) shows the reflectivity spectrum after correction for the reflection of the sapphire substrate while an attenuated total reflection (ATR) spectrum of the hBN sample normalized to the sapphire substrate reflection is presented in Fig. S2(b) (symbols). The latter displays a peak absorption of 6 % at 1366.7 cm^{-1} and a spectral width of $\Delta\nu \approx 15 \text{ cm}^{-1}$ (FWHM).

The measured reflectivity spectrum in Fig. S2(a) was analyzed using the transfer matrix method based on the Fresnel equations [2, 3]. We consider a 2.5 nm-thick hBN film with the c -axis perpendicular to the sample surface, sandwiched be-

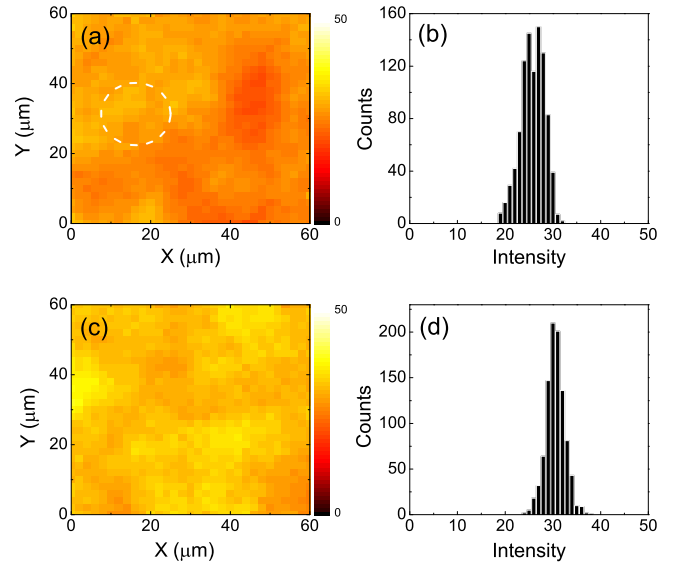


FIG. S1. (a) Spatially resolved second-harmonic intensity from the few-layer hBN sample. The signal is averaged over a circular spot of $18 \mu\text{m}$ radius (white circle), the total area shown is $60 \times 60 \mu\text{m}^2$. The sample was scanned with a $2 \mu\text{m}$ spot size. (b) Intensity histogram of the data in panel (a). (c,d) Second harmonic map and histogram measured at a different sample position.

tween air and sapphire. The refractive index of sapphire was taken from Ref. [4]. The dielectric function of hBN in the range of the TO and LO phonon resonances is modeled by the classical oscillator form as

$$\epsilon(\omega) = \epsilon_\infty \left(1 + \frac{\omega_{\text{LO}}^2 - \omega_{\text{TO}}^2}{\omega_{\text{TO}}^2 - \omega^2 - i\gamma\omega} \right) \quad (1)$$

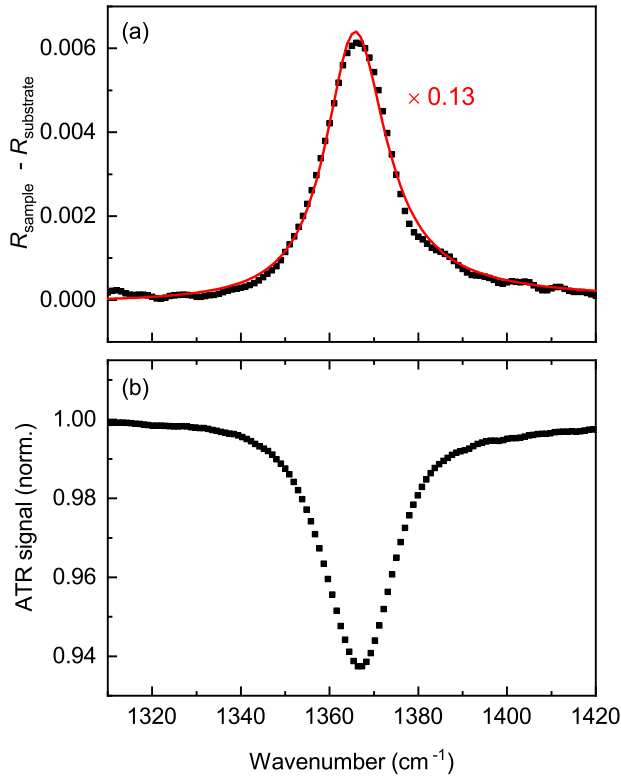


FIG. S2. (a) Linear reflectivity spectrum of the hBN sample after correction for the reflectivity of the sapphire substrate (symbols) and scaled numerical fitting curve (scaling factor 0.13, red line). (b) Attenuated total reflectance (ATR) spectrum of the sample normalized to the reflection of the sapphire substrate.

TABLE S1. Parameter values derived from the numerical fit of the linear reflectivity spectrum.

Light field \mathbf{E}	ϵ_∞	ω_{TO}	ω_{LO}	γ
s -polarization ($\mathbf{E} \perp c$ -axis)	4.6	1365.3	1603.6	14.3
p -polarization ($\mathbf{E} \parallel c$ -axis)	4.6	1365.3	1603.6	14.3
p -polarization ($\mathbf{E} \parallel c$ -axis)	2.95	760	825	3

where ω_{LO} and ω_{TO} are the LO and TO phonon frequencies, γ is the damping constant determining the spectral width of the TO phonon resonance, and ϵ_∞ is the high-frequency dielectric constant. A single oscillator term determines the dielectric function for s -polarization of the incoming light (in-plane for the hBN sample), while a second term with phonons at lower frequency is present for p -polarization [3]. The solid line in Fig. S2(a) represents a calculated spectrum scaled to the experimental spectrum. This least-square fit gives the parameter values summarized in Table S1. Similar to the results of Ref. 2 for thin-layer samples, the peak value of the calculated reflectivity is substantially higher than the experimental value, in the present case by a factor of 7.7.

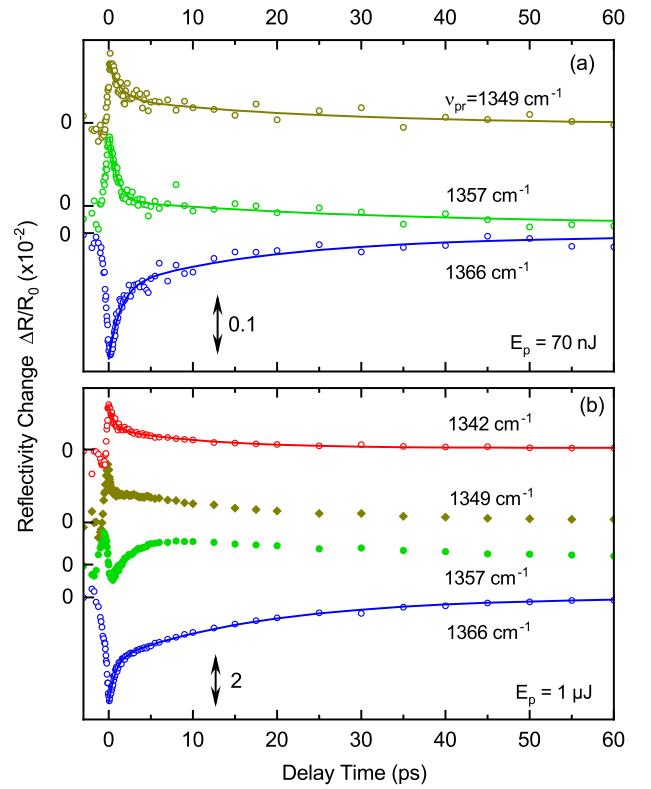


FIG. S3. (a) Time-resolved transients of reflectivity changes measured with pump pulses of an energy of (a) $E_p = 70$ nJ and (b) $E_p = 1$ μJ . Data (symbols) are shown for a 60-ps range of delay time and the same probe frequencies as in Fig. 2 of the article. The solid lines represent bi-exponential fitting curves with two instantaneously rising signal components which decay with time constants of 1.2 and 22 ps.

FEMTOSECOND PUMP-PROBE METHOD

The time-resolved experiments are based on a temporally and spectrally resolved pump-probe approach with femtosecond mid-infrared pulses. As shown in Fig.1(b) (inset) of the article, s -polarized pump and probe pulses are reflected from a gold-coated prism and hit the sample under different angles of incidence. The diameter of the overlapping pump and probe spots was approximately 150 μm , the angle of incidence of the probe some 20°. The probe beam reflected from the second facet of the prism is spectrally dispersed in a monochromator, and detected with a 64-element HgCdTe detector array (spectral resolution 2 cm^{-1}). A reference pulse reflected from an unexcited part of the sample is detected by a second array.

Pump pulses centered around 1400 cm^{-1} and probe pulses covering the 1200 to 1800 cm^{-1} range were generated in two optical parametric amplifiers driven by a Ti:sapphire laser system [5]. The pump energy E_p was varied between 70 nJ and 1.0 μJ , the probe pulses had an energy of 10 nJ. The temporal cross correlation of pump and probe pulses had a width of 150 fs (FWHM). In a separate series of measurements, the

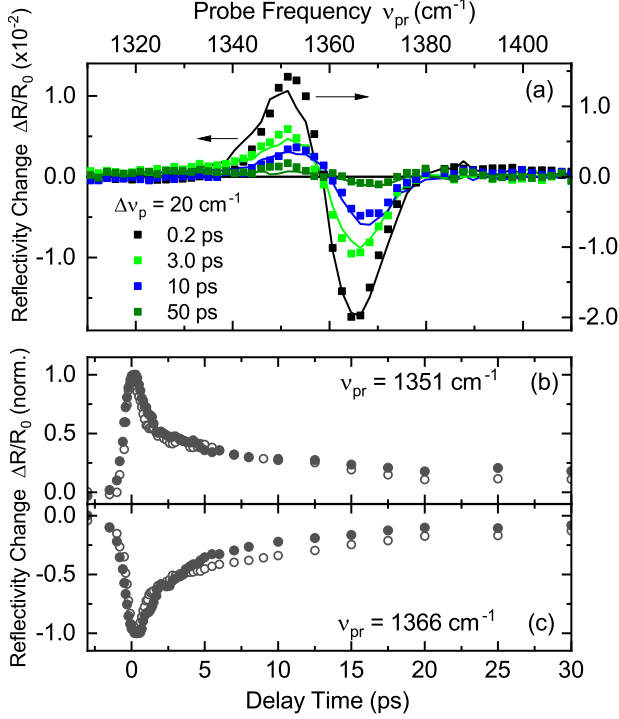


FIG. S4. Pump-probe spectra measured with a reduced pump bandwidth $\Delta\nu_p = 20 \text{ cm}^{-1}$ for different pump-probe delays (symbols, right ordinate scale). The lines represent spectra taken with full pump bandwidth and the same amount of absorbed pump energy (left ordinate scale). (b), (c) Time resolved transients recorded with reduced pump bandwidth (solid symbols) and full pump bandwidth (open symbols) at two probe frequencies ν_{pr} .

pump bandwidth $\Delta\nu_p \approx 200 \text{ cm}^{-1}$ (FWHM) was reduced by bandpass filters to a spectral width (FWHM) of 20, 32, and 54 cm^{-1} . The spectral narrowing to 20 cm^{-1} resulted in a significant temporal broadening of the pump pulse, the width of the cross correlation between pump and probe pulses in this case was 780 fs.

PUMP-PROBE RESULTS

Transient reflectivity spectra of the few-layer hBN sample were measured for delay times up to 60 ps. From such spectra,

$$\Pi_{\mathbf{0}j}^{(L)}(\omega) = \frac{1}{2N\hbar} \sum_{\mathbf{q}, j_1} V^{(4)}(\mathbf{0}j, \mathbf{0}j, -\mathbf{q}j_1, \mathbf{q}j_1)(2n_{\mathbf{q}j_1} + 1), \quad (2)$$

$$\Pi_{\mathbf{0}j}^{(B)}(\omega) = -\frac{1}{2N\hbar^2} \sum_{\mathbf{q}, j_1, j_2} \left| V^{(3)}(\mathbf{0}j, -\mathbf{q}j_1, \mathbf{q}j_2) \right|^2 \left(\frac{2(\omega_{\mathbf{q}j_1} + \omega_{\mathbf{q}j_2})(1 + n_{\mathbf{q}j_1} + n_{\mathbf{q}j_2})}{(\omega_{\mathbf{q}j_1} + \omega_{\mathbf{q}j_2})^2 - (\omega + i\delta)^2} + \frac{2(\omega_{\mathbf{q}j_1} - \omega_{\mathbf{q}j_2})(n_{\mathbf{q}j_2} - n_{\mathbf{q}j_1})}{(\omega_{\mathbf{q}j_2} - \omega_{\mathbf{q}j_1})^2 - (\omega + i\delta)^2} \right). \quad (3)$$

Here, $\mathbf{q}j$ are the phonon quantum numbers (wave-vector

and branch index). The functions $\Pi_{\mathbf{0}j}(\omega)$, associated to the time-dependent reflectivity change $\Delta R/R_0$ at fixed probe frequencies ν_{pr} was derived. Figure S3 shows transients for the same probe frequencies as in Fig. 2 of the article up to a delay time of 60 ps (symbols). The time evolution is reproduced by two signal components, which rise instantaneously upon excitation and decay with time constants of 1.2 and 22 ps (solid lines). The transients at $\nu_{pr} = 1349$ and 1357 cm^{-1} measured with $E_p = 1 \mu\text{J}$ display a nonexponential time evolution, which originates from the spectral shift of the envelopes of the pump-probe spectra.

Additional measurements were performed with pump pulses of a reduced bandwidth $\Delta\nu_p$. The pump energy was adjusted to implement a similar excitation level with and without bandwidth restriction. In Fig. S4(a), pump-probe spectra recorded with $\Delta\nu_p = 20 \text{ cm}^{-1}$ (FWHM, symbols) at different delay times are compared to a data set recorded with the full $\Delta\nu_p = 200 \text{ cm}^{-1}$ (lines, $E_p \approx 400 \text{ nJ}$). The two sets of spectra display very similar spectral envelopes. The absolute signal amplitudes differ slightly because of the different spatial overlap of pump and probe beams in the two measurements. The time-resolved pump-probe traces shown in Figs. S4(b,c) follow the same biphasic decay kinetics for both pump bandwidths. A very similar behavior was observed in measurements with $\Delta\nu_p = 32$ and 54 cm^{-1} .

Comparative pump-probe measurements with a bulk hBN sample in the range of the reststrahlen band from 1350 to 1650 cm^{-1} give a markedly different nonlinear response to be discussed elsewhere.

COMPUTATIONAL APPROACH

Calculations were done entirely from first principles within density functional theory (DFT) [6, 7], with the quantum-espresso package [8] which allows efficient calculation of vibrational [9] and anharmonic properties [10, 11].

Anharmonic shifts and line widths (the inverse of lifetimes) can be obtained from the standard Green's function perturbative approach (see [12, 13] and references therein) as, respectively, the real and imaginary part of the phonon self-energy which, at the lowest order in \hbar , is the sum of the so called "loop" (four-phonons) and "bubble" (three-phonons) diagram contributions:

and branch index). The functions $\Pi_{\mathbf{0}j}(\omega)$, associated to the

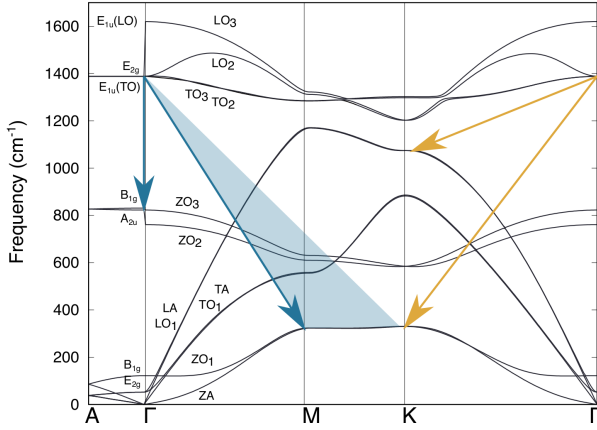


FIG. S5. Phonon dispersion of hBN and TO phonon relaxation pathways

center-zone phonon $\mathbf{0}j$, are evaluated at the phonon angular frequency $\omega = \omega_{\mathbf{0}j}$. The sum is performed on a large uniform grid of N wavevectors on the Brillouin zone, the convergence of which will depend on the value of the small broadening parameter δ . $n_{\mathbf{q}j}$ is the temperature-dependent Bose-Einstein statistics occupation of the phonon $\mathbf{q}j$. $V^{(3)}$ and $V^{(4)}$ are the third- and fourth-order derivatives of the total energy of the crystal \mathcal{E}^{tot} with respect to specific phonon modes. In particular, considering explicitly the dependence $\mathcal{E}^{tot}(\{u_{s\alpha}(\mathbf{R}_l)\})$ on to the atomic displacement $u_{s\alpha}(\mathbf{R}_l)$, from the equilibrium position, of the s -th atom, along the α Cartesian coordinate in the crystal cell identified by the lattice vector \mathbf{R}_l , we use the definition

$$V^{(n)}(\mathbf{q}_1 j_1, \mathbf{q}_2 j_2, \dots, \mathbf{q}_n j_n) = \frac{\partial^n \mathcal{E}^{cell}}{\partial X_{\mathbf{q}_1 j_1}, \partial X_{\mathbf{q}_2 j_2}, \dots, \partial X_{\mathbf{q}_n j_n}} \quad (4)$$

where \mathcal{E}^{cell} is the energy per unit cell and the non-dimensional quantity $X_{\mathbf{q}j}$ is

$$X_{\mathbf{q}j} = \frac{1}{N} \sum_{l,s,\alpha} \sqrt{\frac{2M_s \omega_{\mathbf{q}j}}{\hbar}} z_{\mathbf{q}j}^{s\alpha*} u_{s\alpha}(\mathbf{R}_l) e^{-i\mathbf{q}\cdot\mathbf{R}_l} \quad (5)$$

$z_{\mathbf{q}j}^{s\alpha}$ being the orthogonal phonon eigenmodes normalized to the unit cell and M_s the atomic masses.

Two further terms, which are included in the present calculations, are the frequency shift associated with the lattice thermal expansion (which can be calculated using the quasi-harmonic approximation [14] including zero-point motion effects) and the self-energy component due to isotopic-disorder scattering, calculated using Eq. (11) of Ref. [15].

Computational details

Calculations were done in the local density approximation (LDA) [16] within the pseudopotential [17] and plane-

wave approaches (110 Ry plane-waves cut-off and $12 \times 12 \times 8$ shifted electronic integration grid). These approximations (DFT+LDA) are chosen since they are known to reproduce extremely well the hBN phonon dispersion [3]. The equilibrium lattice parameters of bulk hBN are $a_0 = 2.478 \text{ \AA}$ and $c_0 = 6.425 \text{ \AA}$. Multilayers systems are simulated in a supercell geometry and with the interlayer distances relaxed to equilibrium.

Phonon dynamical matrices were calculated exactly (within DFT) on a uniform $8 \times 8 \times 6$ grid of k-points. The sums on Eqs. (2) and (3) are then done on a finer $100 \times 100 \times 100$ grid on which the matrices are obtained from Fourier interpolation with the standard procedure described in [11]. The calculation of certain terms of Π is not trivial, since one needs to determine the anharmonic phonon-scattering coefficients (APSC) among all the possibly involved phonons. $\Pi^{(B)}$ depends on 3-phonon scattering coefficients and the APSC among three phonons with distinct wavevectors can be calculated with the approach of 10 and 11. The 4-phonons APSC necessary for $\Pi^{(L)}$ can be obtained by finite differentiation as in [12, 13].

Results

In the framework discussed above we evaluate the total relaxation times by including the anharmonic and isotopic contributions for all modes. Values at Γ point are reported in table S2.

Regarding the TO phonon decay discussed in the main text, if we include only 3-phonon scattering processes, it can decay only to two low-energy phonons at K, namely LA (degenerate with LO₁) at 1073 cm^{-1} and ZA (degenerate with ZO₁ at 330 cm^{-1} (yellow line in Fig.S5), because of energy and momentum conservation rules. In addition, as reported in [18] there is also four-phonon decay processes, which consists of the decay into a zone-center A_{2u} mode (at 760.58 cm^{-1}) and a pair of opposite wave-vector ZA - ZO₁ along the M-K line at 330 cm^{-1} (blue line and shaded area in Fig. S5).

From Eq. (4) it is possible to evaluate the anharmonic coupling terms V^3 and V^4 between the TO and the low energy shear modes. As also reported in the main text, in bulk this coupling is weak and with a predominant contribution of 4-phonon processes with a value around -0.02 cm^{-1} . Nevertheless this coupling term displays a strong dispersion along the z-axis and increases up to -2.0 cm^{-1} so that the excitation energy required per unit cell in order to experimentally observe a TO shift $\Delta v_{TO} = 10 \text{ cm}^{-1}$, would be roughly 20 meV, well in the range of the experiment.

Raman Cross Sections

In a N layers slab of a lamellar system, according to the classification of Ref. [19], the low-frequency interlayer vibrational modes (in which the atoms within a single plane translate almost rigidly) can be classified into $(N - 1)$ in-plane

TABLE S2. Phonon frequencies $\nu_{0,j}$ (cm^{-1}) and total relaxation times of optical modes $\tau_{\text{TOT},0,j}$ (ps) at Γ .

	TO ₁	LO ₁	ZO ₁	ZO ₂	ZO ₃	TO ₂	LO ₂	TO ₃	LO ₃
$\nu_{0,j}$	51.83	51.83	121.69	761.02	822.66	1388.41	1388.41	1388.41	1620.27
$\tau_{\text{TOT},0,j}$	25.81	25.81	84.94	12.36	47.17	1.78	1.78	1.78	1.78

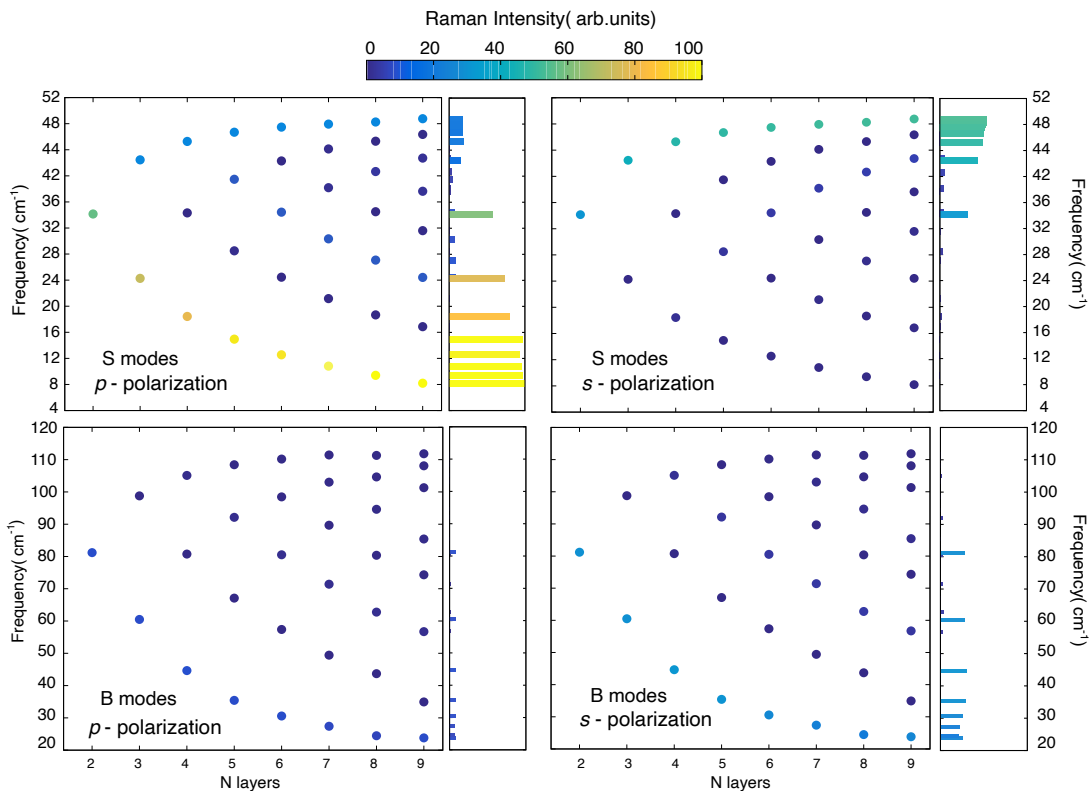


FIG. S6. Calculated Raman cross section intensities in a N layers slab of hBN for shearing S (top panels) and breathing modes B (low panels) for p -polarization and s -polarization. The Raman intensity scale is the same for all 4 cases. For further clarity, on the right-hand side of each panel, the intensity of each dot is also shown as a histogram.

shear (S) and $(N - 1)$ out-of-plane breathing/compression (B) vibration modes. We evaluate here within DFT the frequency range of these modes from 2 to 9 layers showing how, in agreement with Ref. [20] they cover for $N = 9$ a frequency range between 8 and 52 cm^{-1} for the shearing modes and between 20 to 110 cm^{-1} for the breathing modes. We determine also the DFT Raman cross sections intensities following the procedure described in Ref. [21]. Results are reported in Fig. S6. In order to simulate the configurations previously described, we consider the Raman light exchange vector parallel to the c -axis (perpendicular to the plane). Two cases are considered: s -polarization (the light is polarized in the direction perpendicular to the plane of incidence) and p -polarization (the light is polarized parallel to the plane of incidence). An average is made on the two possible in-plane orientations of the sample and on the polarization of the reflected light. The

light is considered incident on the hBN plane at an angle of 45° (note that the s -polarization results do not depend on this angle). As also shown for multilayered graphene and transition metal dichalcogenides in [19] for the shear modes the highest frequency around 50 cm^{-1} (lowest around 8 cm^{-1}) has a cross section for the s -polarization (p -polarization) substantially larger than the other modes at lower (larger) frequencies. For an even number of layers only a subset of the shear modes is Raman-active, while for an odd number of layers all of them are infrared and Raman active. Differently from the shearing modes, for the breathing modes the lowest frequency curve (around 20 cm^{-1} at $N = 9$) has always a larger cross section than higher frequency modes. Interestingly, the anharmonic coupling between TO and breathing modes is of the same order of magnitude as that of TO with shear modes.

* elsasser@mbi-berlin.de

- [1] R. Page, J. Casamento, Y. Cho, S. Rouvimov, H. G. Xing, and D. Jena, Rotationally aligned hexagonal boron nitride on sapphire by high-temperature molecular beam epitaxy, *Phys. Rev. Mater.* **3**, 064001 (2019).
- [2] J. D. Caldwell, A. V. Kretinin, Y. Chen, V. Giannini, M. M. Fogler, Y. Francescato, C. T. Ellis, J. G. Tischler, C. R. Woods, A. J. Giles, M. Hong, K. Watanabe, T. Taniguchi, S. A. Maier, and K. S. Novoselov, Sub-diffractive volume-confined polaritons in the natural hyperbolic material hexagonal boron nitride, *Nature Comm.* **5**, 5521 (2014).
- [3] A. J. Giles, S. Dai, I. Vurgaftman, T. Hoffman, S. Liu, L. Lindsay, C. T. Ellis, N. Assefa, I. Chatzakis, T. L. Reinecke, J. G. Tischler, M. M. Fogler, J. H. Edgar, D. N. Basov and J. D. Caldwell, Ultralow-loss polaritons in isotopically pure boron nitride, *Nature Mat.* **17**, 134 (2018).
- [4] M. R. Querry, Optical Constants, Contractor Report CRDC-CR-85034 (1985)
- [5] N. E. Levinger, R. Costard, E. T. J. Nibbering, and T. Elsaesser, Ultrafast energy migration pathways in self-assembled phospholipids interacting with confined water, *J. Phys. Chem. A* **115**, 11952 (2011).
- [6] P. Hohenberg and W. Kohn, Inhomogeneous electron gas, *Phys. Rev.* **136B**, 864 (1964).
- [7] W. Kohn and L. J. Sham, Self-consistent equations including exchange and correlation effects, *Phys. Rev.* **140A**, 1133 (1965).
- [8] P. Giannozzi, O. Andreussi, T. Brumme, O. Bunau, M. Buongiorno Nardelli, M. Calandra, R. Car, C. Cavazzoni, D. Ceresoli, M. Cococcioni, N. Colonna, I. Carnimeo, A. Dal Corso, S. de Gironcoli, P. Delugas, R. DiStasio, A. Ferretti, A. Floris, G. Fratesi, G. Fugallo, R. Gebauer, U. Gerstmann, F. Giustino, T. Gorni, J. Jia, M. Kawamura, H. Y. Ko, A. Kokalj, E. Küçükbenli, M. Lazzeri, M. Marsili, N. Marzari, F. Mauri, N. L. Nguyen, H. V. Nguyen, A. Otero-de-la-Roza, L. Paulatto, S. Poncè, D. Rocca, R. Sabatini, B. Santra, M. Schlipf, A. P. Seitsonen, S. Smogunov, I. Timrov, T. Thonhauser, P. Umari, N. Vast, and S. Baroni, Advanced capabilities for materials modelling with Quantum ESPRESSO, *J. Phys.: Condens. Matter* **29**, 465901 (2017).
- [9] S. Baroni, S. de Gironcoli, A. Dal Corso, and P. Giannozzi, Phonons and related crystal properties from density-functional perturbation theory, *Rev. Mod. Phys.* **73**, 515 (2001).
- [10] M. Lazzeri and S. de Gironcoli, First-principles study of the thermal expansion of Be(10 $\bar{1}$ 0), *Phys. Rev. B* **65**, 245402 (2002).
- [11] L. Paulatto, F. Mauri, and M. Lazzeri, Anharmonic properties from a generalized third-order *ab initio* approach: Theory and applications to graphite and graphene, *Phys. Rev. B* **87**, 214303 (2013).
- [12] M. Lazzeri, M. Calandra, and F. Mauri, Anharmonic phonon frequency shift in MgB₂, *Phys. Rev. B* **68**, 220509(R) (2003).
- [13] G. Fugallo, B. Rousseau, and M. Lazzeri, Infrared reflectance, transmittance, and emittance spectra of MgO from first principles, *Phys. Rev. B* **98**, 184307 (2018).
- [14] B. B. Karki, R. M. Wentzcovitch, S. de Gironcoli, and S. Baroni, High-pressure lattice dynamics and thermoelasticity of MgO, *Phys. Rev. B* **61**, 8793 (2000).
- [15] S. I. Tamura, Isotope scattering of dispersive phonons in Ge, *Phys. Rev. B* **27**, 858 (1983).
- [16] J. P. Perdew and A. Zunger, Self-interaction correction to density-functional approximations for many-electron systems, *Phys. Rev. B* **23**, 5048 (1981).
- [17] N. Troullier and J. L. Martins, Efficient pseudopotentials for plane-wave calculations, *Phys. Rev. B* **43**, 1993 (1991).
- [18] R. Cuscó, B. Gil, G. Cassabois, and L. Artús, Temperature dependence of Raman-active phonons and anharmonic interactions in layered hexagonal BN, *Phys. Rev. B* **94**, 155435 (2016).
- [19] L. Liang, A. A. Puretzy, B. G. Sumpter, and V. Meunier, Interlayer bond polarizability model for stacking-dependent low-frequency Raman scattering in layered materials, *Nanoscale* **9**, 15340 (2017).
- [20] K. H. Michel and B. Verberck, Theory of rigid-plane phonon modes in layered crystals, *Phys. Rev. B* **85**, 094303 (2012).
- [21] M. Lazzeri and F. Mauri, First-Principles Calculation of Vibrational Raman Spectra in Large Systems - Signature of Small Rings in Crystalline SiO₂, *Phys. Rev. Lett.* **90**, 036401 (2003).